An optimal design of thermal-actuated and piezoresistive-sensed CMOS-MEMS resonant sensor

2013 J. Micromech. Microeng. 23 115015

(http://iopscience.iop.org/0960-1317/23/11/115015)

J. Micromech. Microeng. **23** (2013) 115015 (13pp) doi:10.1088/0960-1317/23/11/115015

An optimal design of thermal-actuated and piezoresistive-sensed CMOS-MEMS resonant sensor

Chun-Chieh Wang[1], **Chun-Yin Tsai**[1], **Tsung-Lin Chen**[1] **and Sin-Hao Liao**[2]

[1] Department of Mechanical Engineering, National Chiao Tung University, Hsinchu, Taiwan, People's Republic of China
[2] National Chip Implementation Center (CIC), South Region Office, National Applied Research Laboratories (NARL), Taiwan, People's Republic of China

E-mail: adamgw1012.me01g@nctu.edu.tw, tsunglin@mail.nctu.edu.tw and shliao@cic.narl.org.tw

Received 4 June 2013, in final form 13 September 2013
Published 21 October 2013
Online at stacks.iop.org/JMM/23/115015

Abstract

This paper proposes an optimal design of the thermal-actuated, piezoresistive-sensed resonator fabricated by a foundry-provided CMOS-MEMS process. The optimal design is achieved both by quantitatively comparing the mechanical properties of different composite films as well as by deriving an analytical model for determining the device dimensions. The analytical model includes a stress model of an asymmetric mechanical structure and a piezoresistivity model of the heavily doped, n-type polysilicon film. The analytical model predicts that the optimal length of the displacement sensor is 200 μm when the thermal actuator is 200 μm in length and the absorption plate is 100 μm in length. Additionally, the model predicts the resistivity of the polysilicon film of (6.8 ± 2.2) mΩ cm and the gauge factor of (6.8 ± 2.9) when the grain size is (250 ± 100) nm. Experimental results agree well with simulation results. Experimental data show that the resonant frequency of the device is 80.06 kHz and shifts to 79.8 kHz when a brick of Pt mass is deposited on the resonator. The mass of the Pt estimated from the frequency shift is 4.5419×10^{-12} kg, while estimated from the measured dimension is 4.4204×10^{-12} kg. Sensitivity of the resonant sensor is calculated to be 1.8×10^{2} Hz ng^{-1}. Experimental results further show that the polysilicon film used in the experiments has a grain size of (241 ± 105) nm, an average gauge factor of 5.56 and average resistivity of 5.5 mΩ cm.

(Some figures may appear in colour only in the online journal)

1. Introduction

Micromachined resonant sensors with the resonant frequency modulated by the measurand have the advantages of high measurement accuracy and quasi-digital output [1]. These sensors have substantially been applied to various sensor applications, including proximity sensing [1], acceleration measurement [2] and bio-molecular detection [3]. Given that a resonant sensor consists of device actuation and motion sensing, the general concerns of designing/fabricating such devices are the process capabilities of implementing those two functionality and feedthrough between the driving node and sensing node [4, 5].

The heavily doped, n-type polysilicon film is a standard gate material in the MOS fabrication process, which can also be used in many MEMS applications. For example, this film can be used as a polysilicon heater for the thermal actuation [6, 7] and a piezoresistor for the strain sensing [4, 8]. Therefore, thermal-actuated and/or piezoresistive-sensed MEMS devices can be realized using standard CMOS process plus post-CMOS process [4]. Other frequently adopted techniques in the CMOS-MEMS process include electrostatic actuation and capacitive sensing. In contrast to those techniques, the thermal-actuated, piezoresistive-sensed approach is characterized by its absence of tiny gaps, hermetic sealing and low actuation voltage, thus making it attractive for use in CMOS-MEMS

designs [4]. However, the piezoresistivity of the polysilicon film largely depends on its fabrication process and is not fully disclosed to MEMS designers, thus limiting the application of polysilicon films in MEMS designs [7].

A considerable amount of literatures of the piezoresistive films have focused on the medium-doped, p-type single crystalline silicon, owing to its large sensitivity in strain sensing [9]. Despite having a lower piezoresistivity than that of single crystalline silicon, polycrystalline silicon can be deposited at lower temperature and is easily integrated with other fabrication process. Consequently, the piezoresistivity of the polysilicon has received increasing attention following the increasing interest in MEMS devices. Reported data in literatures are not directly applicable in predicting the piezoresistivity of the polysilicon film in a standard MOS process not only because the piezoresistivity of the polysilicon film depends on the grain size, texture and doping concentration [10], but also because most of the reported data are for the medium–low doping concentration, p-type silicon. For example, when modeling the hole density of a p-type silicon film, many studies approximate the Fermi–Dirac distribution by using the Boltzmann distribution. This approximation may be inapplicable to a heavily doped n-type silicon film [11].

Designing MEMS devices with industrial CMOS processes is attractive for its cost reduction, high device yield and on-chip circuitry [12]. However, engineers may find it extremely challenging to optimize the MEMS device performance because the fabrication process has been tuned exclusively for IC circuitry. Since the fabrication process is fixed, MEMS designers can only select the appropriate layers and devise device dimensions to achieve the optimal performance. Previous MEMS research with standard MOS fabrication process often omits the discussion of layer selection because the selection is rather limited as compared to the intended MEMS functionality. For example, when using PolyMUMPs or double-metal CMOS process to fabricate MEMS resonators, the films available for making MEMS devices can only fulfil the requirements of the device actuation and motion sensing [1, 13, 14]. However, as the CMOS process used becomes increasing complex, more than one layer can be used to implement the intended MEMS functions. In that case, the selected layers affect the structure thickness, thermal conductivity and ultimately change the performance of the MEMS devices.

This work presents an optimal design of the thermal-actuated, piezoresistive-sensed resonant sensor fabricated by a foundry-provided CMOS-MEMS process. Owing to that the fabrication process is fixed, this design is optimized by both quantitatively examining the appropriate layers and deriving an analytical model for determining the device dimensions. This analytical model includes the stress analysis of a three-piece mechanical structure and a piezoresistivity model of the heavily doped, n-type polysilicon film. The piezoresistivity model is obtained by rewriting the equations of a resistance model [15, 16] and a piezoresistivity model [9, 10] of the medium-doped, p-type polysilicon. Therefore, this model is capable of predicting the device actuation and piezoresistive motion sensing of the resonator. The design procedures, feedthrough problem, and testing results are discussed in detail.

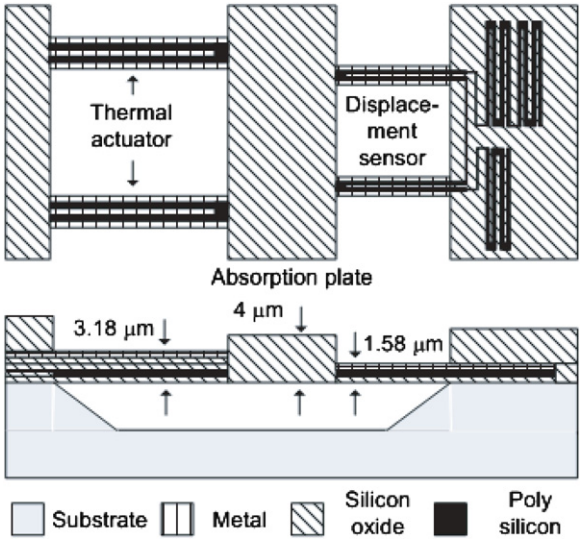

Figure 1. A conceptual design of the proposed resonant sensor.

2. Conceptual design

Figure 1 shows the conceptual design of the devised resonant sensor. It consists of a 'thermal actuator', 'absorption plate' and 'displacement sensor'. The thermal actuator drives the device into resonance. The absorption plate provides a platform for the bio-chemical reactions, thus changing the mass of the entire system (resonator). Resonant frequency of the device is shifted by the additional mass and is measured by analyzing the readout signal of the displacement sensor. The resonant frequency change due to the gravimetric change ($\triangle m$) can be modeled as [17]

$$\triangle m = m_0 \left(\frac{\omega_n^2}{\omega_n'^2} - 1 \right), \tag{1}$$

where ω_n and ω_n' are the resonant frequencies of the resonator before and after the mass absorption; m_0 is the original mass of the device.

2.1. Foundry-provided CMOS-MEMS process

The fabrication processes of this sensor design are the TSMC® 2P4M process and the post-CMOS process provided by the National Chip Implementation Center [7]. The 2P4M process mainly consists of two n-type polysilicon films (poly1, poly2), four metal films (aluminum, metal1∼4) and dielectric films (oxide) in between each metal film. The process profile and film thickness are shown in figure 2.

The post-CMOS process defines/releases the MEMS structure without damaging the circuitry. These actions are achieved by defining the MEMS structures using an anisotropic oxide etch and release the structure using an isotropic silicon etch. Since the metal layer is an etch stop for the oxide etch and the oxide layer is an etch stop for the silicon

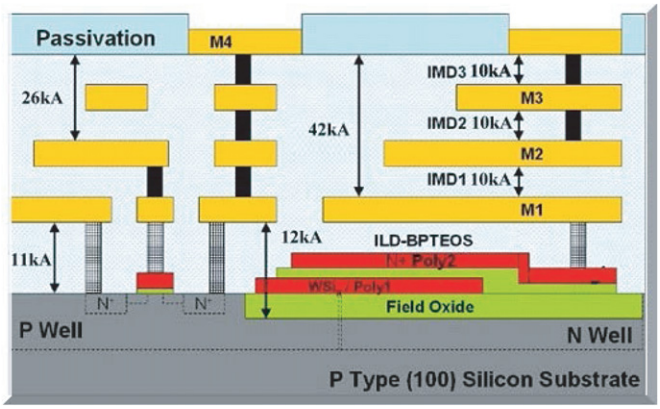

Figure 2. TSMC® 2P4M process. It is a standard CMOS process and consists of two polysilicon films and four metal films.

etch, the polysilicon film in a suspended MEMS structure must be covered by a metal film on the top and an oxide film at the bottom.

According to the data sheet of the 2P4M process, the sheet resistance of poly1 is 8Ω/*square* and poly2 is 50Ω/*square*. Therefore, poly1 is suitable for implementing the heater in the thermal actuator, while poly2 is suitable for implementing the piezoresistor in the displacement sensor. However, based on our experiences, the poly1 layer is often damaged during the post-CMOS process. Only poly2 layers are used when polysilicon films are needed in the design. Moreover, the metal4 layer is not used in this sensor design for the same reason.

2.2. Design of the thermal actuator

The design goal of the thermal actuator is generating a large displacement when a voltage is applied. Therefore, this thermal actuator must consist of a resistive film to generate sufficient heat dissipation. Additionally, the structure must have a low thermal conductivity, low bending stiffness and a multi-layer structure with large mismatched thermal coefficients to convert the joule heating into structure deflection. To satisfy the above requirements, the thermal actuator is designed as a multi-layer structure and the incorporated layers are determined by using finite-element method (FEM) simulations.

Figure 3 show five designs with different layer combinations of the thermal actuator. In type I, the thermal actuator consists of metal2-oxide-metal1-oxide-poly2-oxide, in which the total layer thickness is 3.72 μm and the width of the poly2 film is designed to be 5 μm. Type II has the same composite structure as that of type I, except for that the poly2 width is 2.5 μm. Type III is similar to type I, except for that the oxide between metal1 and metal2 is replaced with many 'via' pillars. Type IV is similar to type I, except for that the metal1 layer is replaced with oxide. In contrast to type IV design, type V has an additional metal3 and oxide layer. All these designs comply with the design rules of the 2P4M process.

In the following FEM simulations, the thermal actuator is 200 μm in length and 20 μm in width. The actuation voltage is 2 volts. Table 1 lists the material properties needed for these simulations. FEM simulation results shown in table 2 indicate that type IV has the largest deflection under the same actuation voltage. Type IV is chosen to be the composite structure for the proposed thermal actuator design. According to the data sheet of the 2P4M process, thickness of this composite structure is 3.18 μm.

2.3. Design of the absorption plate

The absorption plate provides a platform for the bio-chemical reactions. It is designed to have a large area, high thermal resistance and large bending stiffness. The large area facilitates more bio-chemical reactions and improves the device sensitivity. The high thermal resistance prevents the heat generated by the thermal actuator from interferencing with the piezoresistive displacement sensor. The large bending stiffness amplifies the structure deflection generated by the thermal actuator, which also improves the device sensitivity. To meet above three requirements, the composite structure of the absorption plate is designed by stacking all the oxide layers without metal layers, leading to a total thickness close to 4.0 μm.

2.4. Design of the piezoresistive displacement sensor

Piezoresistive displacement sensor uses the piezoresistivity of the polysilicon film for strain sensing. It is designed to have a low bending stiffness so that it would not destruct the

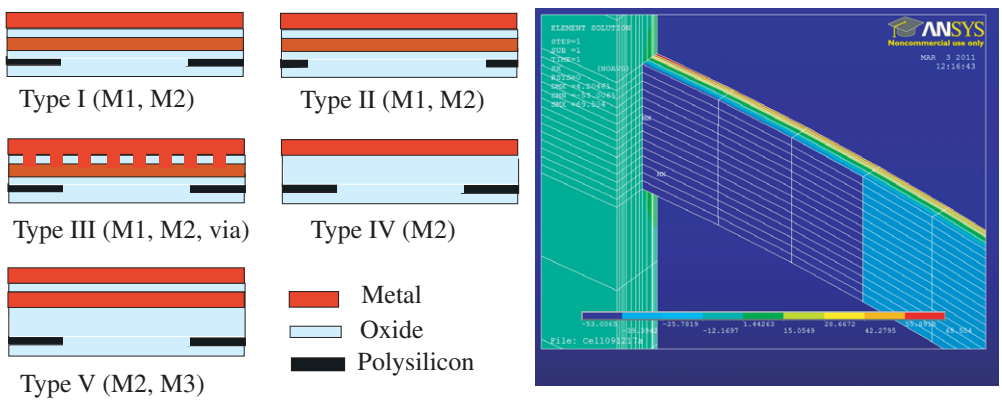

Figure 3. Five designs of thermal actuators. Each design has different composite structure.

Table 1. Material properties (Young's modulus E, Poisson's ratio ν and density ρ), thermal conductivity κ and specific heat capacity (c) used for modeling the proposed resonant sensor.

Material	E (GPa)	ν	ρ(kg m^{-3})	κ (Wm^{-1}K^{-1})	c(Jkg^{-1}K^{-1})
Polysilicon	169	0.27	2 330	25	700
Silicon oxide	70	0.25	2 200	0.059	840
Aluminum	70	0.33	2 700	237	898.7
Tungsten	410	0.28	19 250	178	242.7
Platinum	170	0.39	21 440	73	132.51

Table 2. FEM simulation results of five thermal actuator designs.

Type	Composite films	Temperature increase (°C)	Total thickness (μm)	Max. deflection (μm)
Type I	metal2/oxide/ metal1/poly2/oxide	33.863	3.72	2.303
Type II	Half poly2	26	3.72	2.059
Type III	metal2/via/ metal1/poly2/oxide	31.15	3.72	2.5
Type IV	metal2/oxide/ oxide/poly2/oxide	37.3	3.18	3.098
Type V	metal3/oxide/metal2 oxide/poly2/oxide	40.7086	4.72	1.727

deflection generated by the thermal actuator. Its composite structure is thus designed to consist of metal1-oxide-poly2-oxide films, resulting in a total thickness close to 1.58 μm. Three additional resistors are also designed using the poly2 layer and located at the fixed substrate. These three resistors along with the piezoresistor in the displacement sensor form a Wheatstone bridge which converts the resistance variation of the piezoresistor into voltage. For the best sensitivity of the bridge output [18], three resistors are designed to have the same resistance as that of the piezoresistor in the displacement sensor.

3. Analytical modeling of the thermal-actuated, piezoresistive-sensed resonator

A previous section discusses the layer selection for the resonant sensor design, which determines the structure thickness of each key component. This section derives a mathematics model for the proposed sensor design for use in further determining the device dimensions and achieving an optimal performance.

3.1. Stress analysis of the resonant sensor

For the stress analysis, the proposed design can be considered as a three-piece structure under the bending moment generated by the thermal actuator. As shown in figure 4(a), from the left to right, each block represents the thermal actuator, absorption plate and displacement sensor. Since the lateral force generated by the thermal actuator contributes less in the structure deformation, the lateral force is ignored. Therefore, the force balance in the y-direction and moment balance in the z-direction can be written as follows:

$$M_L - M_P - M_R + V_R(L_1 + L_2 + L_3) = 0$$
$$V_L = V_R, \quad (2)$$

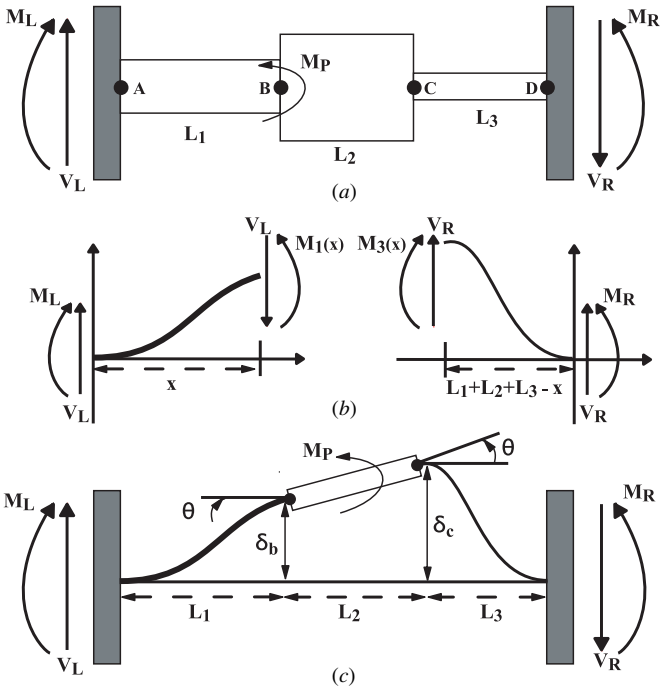

Figure 4. A schematic of the stress analysis of the proposed sensor design. (a) A free-body diagram of the overall system. (b) Free-body diagrams of the thermal actuator and displacement sensor. (c) Boundary conditions of the three-piece structure.

where M_P is the moment generated by the thermal actuator; M_R and M_L are the reaction moments at two fixed ends; V_L and V_R are the shear forces at two fixed ends; L_1, L_2 and L_3 are the lengths of the thermal actuator, absorption plate and displacement sensor, respectively.

If the absorption plate is sufficiently rigid, deformation of the absorption plate can be ignored. Stress analysis can thus be simplified by separating them for the thermal actuator

and displacement sensor. By using the free-body diagram (see figure 4(*b*)), the displacement in *y*-direction can be modeled as follows:

$$(EI)_1 \frac{d^2 y_1}{dx^2} = M_1(x) = V_L x + M_L$$

$$(EI)_3 \frac{d^2 y_3}{dx^2} = M_3(x) = M_R - V_R(L_1 + L_2 + L_3 - x), \qquad (3)$$

where $(EI)_1$ and $(EI)_3$ are the equivalent bending property of the thermal actuator and displacement sensor, respectively. The above equations are linked together by the following boundary conditions:

$$\begin{aligned}
&y_1(x)|_{x=0} = 0 \\
&\left.\frac{dy_1(x)}{dx}\right|_{x=0} = 0 \\
&y_3(x)|_{x=L_1+L_2+L_3} = 0 \\
&\left.\frac{dy_3(x)}{dx}\right|_{x=L_1+L_2+L_3} = 0 \\
&\left.\frac{dy_1(x)}{dx}\right|_{x=L_1} = \left.\frac{dy_3(x)}{dx}\right|_{x=L_1+L_2} = \theta \\
&y_3(x)|_{x=L_1+L_2} = y_1(x)|_{x=L_1} + L_2 \cdot \theta. \qquad (4)
\end{aligned}$$

The bending moment M_p is generated by the thermal actuator which is a composite structure of metal-oxide-poly-oxide films. Since the poly film in this composite structure is much thinner than other films, the bending moment can be approximated as the mismatch of the thermal coefficients between the metal film and oxide film. Based on the analysis of a bi-morphs structure [19], the bending moment M_p can be approximated as

$$M_p = w \cdot (t_m d_m E_m \alpha_m - t_o d_o E_o \alpha_o \cdot) T \qquad (5)$$

where the subscript m, o stands for the metal and oxide, respectively; w is the width of the thermal actuator; t is the film thickness; E is the Young's modulus of the film; d is the distance from respective film to the neutral axis of the composite structure and α is the thermal coefficient.

3.2. Piezoresistivity of the heavily doped, n-type polysilicon

According to Lu *et al* [15], the resistivity of a polysilicon film is contributed by two sources: potential barrier at the grain boundary and the bulk resistivity of the crystalline. Energy difference between the grain boundary and crystalline region results in an energy barrier and depletion region in the vicinity of the grain boundary. If the crystalline region is not completely depleted ($L_g > 2\omega_g$, see figure 5), the resistivity of a polysilicon film (ρ_t) can be modeled as

$$\rho_t = \frac{L_g - (2\omega_g + \delta)}{L_g}\rho_g + \frac{(2\omega_g + \delta)}{L_g}\rho_b \qquad (6)$$

where L_g is the average grain size; ω_g is the depletion width; ρ_g is the resistivity in the grain region; ρ_b is the resistivity due to the grain boundary and δ is the width of the grain boundary.

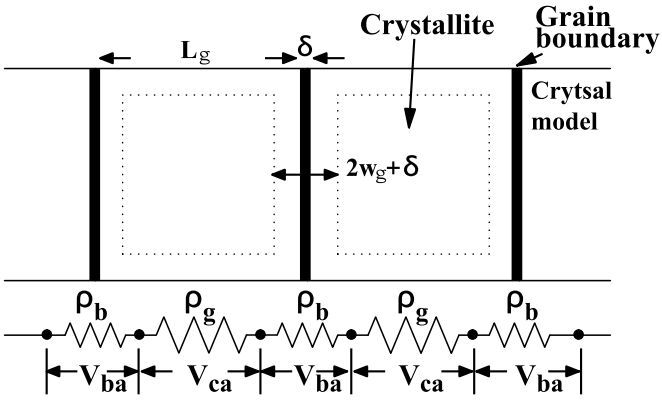

Figure 5. A simple electrical model for one-dimensional grain structure of the polysilicon [8].

The resistivity of the grain region equals to that of the single crystalline silicon, which can be modeled as [20]:

$$\rho_g = \frac{1}{qn(0)\mu_n}, \qquad (7)$$

where q is the elementary charge; $n(0)$ is the electron concentration in the charge neutral region of the grain and μ_n is the electron mobility. By applying the thermionic-emission theory to model the conductivity of the gain boundary [15], the current density J of an n-type film can be written as

$$J = 2fqn(0)\left(\frac{1}{2m_e^* KT}\right)^{1/2} \exp\left(\frac{-qV_B}{KT}\right) \sinh\left(\frac{qV_{ba}}{2KT}\right)$$

$$V_B = \frac{qn(0)\omega_g^2}{2\epsilon}, \qquad (8)$$

where m_e^* is electron effective mass; V_B is the bending of the energy band diagram due to the energy difference between grain boundary and the grain; f is an artificial factor to fit experimental data; K is the Boltzmann constant; T is the temperature in kelvin; V_{ba} is the voltage drop across grain boundary and ϵ is the dielectric constant of the silicon.

Depletion width is related to the energy level of the grain boundary. The depletion width can be determined by using the concept of ionized trap density (Q_T) at the grain boundary and the charge-neutrality condition, which equates the number of ionized dopants in the depletion region to the number of the charge traps in the grain boundary (see equation (9))

$$2n(0)\omega_g = Q_T, \qquad (9)$$

where the trap density Q_T can be obtained from the experimental data [15].

If the film is heavily doped (i.e., more than 1×10^{-20} cm^{-3} in this case), the Fermi level and electron concentration should be calculated directly from the Fermi–Dirac distribution but not the approximation of the Boltzmann distribution. Alternatively, the electron concentration can be approximated by the impurity concentration N_d by assuming that the impurity is totally ionized [15]. Additionally, when the voltage drop $V_{ba} \ll \frac{2KT}{q}$, the barrier resistivity of the n-type film described in equation (8) can be simplified as

$$\rho_b = \frac{V_{ba}}{J(2\omega_g)} \simeq \frac{1}{f}\frac{1}{2\omega_g q^2 N_d}(2\pi m_e^* KT)^{1/2} \exp\left(\frac{qV_B}{KT}\right). \qquad (10)$$

Once the doping concentration, average grain size, boundary width and trap density are known, the resistivity of a heavily doped, n-type polysilicon film can be calculated using equations (6)–(10).

3.3. Gauge factor of the polysilicon film

Gauge factor (G) denotes the sensitivity of a strain sensor, which is defined as the relative change in resistance $\triangle R/R$ per unit strain ε.

$$G = \frac{1}{\epsilon}\frac{\Delta R}{R} = 1 + 2\nu + \frac{\Delta\rho}{\rho\varepsilon}, \tag{11}$$

where ν is Poisson's ratio and ρ is the resistivity. The first two terms represent the change in resistance due to dimensional changes, while the last term represents the change in resistivity due to strain. For anisotropic piezoresistive materials, the last term in the longitudinal direction (i.e., in the direction of the stress applied) can be modeled as

$$\begin{aligned}\frac{\Delta\rho}{\rho\varepsilon} &= \frac{\pi_l}{S_{11}}\\ \pi_l &= \pi_l|_{T=300\,\mathrm{K}}\dot{P}(N_d, T),\end{aligned} \tag{12}$$

where π_l is the piezoresistance coefficient in the direction of stress applied; S_{11} denotes the equivalent compliance in the direction of stress applied; $P(N_d, T)$ describes the dependence of piezoresistance on the impurity concentration and temperature. The values of $P(N_d, T)$ are often obtained experimentally and can be found in [9].

Relation between the principle axis of the anisotropic material and the longitudinal direction of the piezoresistance can be described by the Euler angles (ϕ, θ, ψ) in a rotation order of z–y–z. In that case, the longitudinal piezoresistance coefficient and the longitudinal compliance can be obtained as [9]

$$\begin{aligned}\pi_l|_{T=300\,\mathrm{K}} &= \pi_{11} + 2(\pi_{44} + \pi_{12} - \pi_{11})\left(l_1^2m_1^2 + l_1^2n_1^2 + m_1^2n_1^2\right)\\ S_{11} &= s_{11} + (s_{44} + 2s_{12} - 2s_{11})\left(l_1^2m_1^2 + l_1^2n_1^2 + m_1^2n_1^2\right)\\ l_1 &= \cos\phi\cos\theta\cos\psi - \sin\phi\sin\psi\\ m_1 &= \sin\phi\cos\theta\cos\psi + \cos\phi\sin\psi\\ n_1 &= -\sin\theta\cos\psi,\end{aligned} \tag{13}$$

where s_{ij} and π_{ij} are the compliance coefficients and piezoresistance coefficients of single crystalline silicon along its principle axis. Their values can be found in [9]. The piezoresistivity of a polysilicon film can be estimated from that of a single crystalline film by assuming that the grain orientation is randomly distributed and the piezoresistive effect is dominated by the resistance in the grain region. In that case, the gauge factor of a polysilicon film can be written as [10]:

$$\begin{aligned}G &= 1 + 2\nu + \frac{\rho_g\langle\pi_l/S_{11}\rangle}{[\rho_g + (2\omega_g + \delta)\rho_b/(L_g - (2\omega_g + \delta))]}\\ \langle\pi_l/S_{11}\rangle &= \left.\frac{\int_{\theta=0}^{\pi/2}\int_{\phi=0}^{\pi/4}(\pi_l/S_{11})\,\mathrm{d}\theta\,\mathrm{d}\phi}{\int_{\theta=0}^{\pi/2}\int_{\phi=0}^{\pi/4}\mathrm{d}\theta\,\mathrm{d}\phi}\right|_{\psi=0},\end{aligned} \tag{14}$$

where $\langle\pi_l/S_{11}\rangle$ is the average value of π_l/S_{11} over all possible directions.

Again, once the grain size, boundary width and the trap density of a polysilicon film are obtained, the gauge factor of a polysilicon film can be predicted using equations (12)–(14).

3.4. Piezoresistive displacement sensor output

Once the gauge factor of a piezoresistive film is known, the resistance variation $\triangle R/R$ due to the strain of the film can be calculated using equation (11). In this case, the piezoresistive film is embedded in the section of the displacement sensor. The strain of the piezoresistive film can be estimated as follows:

$$\varepsilon(x) = \frac{M_3(x)t_z}{(EI)_3}, \tag{15}$$

where t_z is the distance between the location of the piezoresistive film and the neutral axis of the composite structure of the displacement sensor. The mean strain of this piezoresistive film is obtained by the integration over the length of the piezoresistive film.

$$\varepsilon_{\mathrm{mean}} = \frac{1}{L_3}\int_0^{L_3}\varepsilon(x)\,\mathrm{d}x = \frac{t_z}{L_3(EI)_3}\int_0^{L_3}M_3(x)\,\mathrm{d}x. \tag{16}$$

Resistance variation of the piezoresistive film is converted into voltage by using a Wheatstone bridge. As discussed previously, three additional resistors are designed to have the same resistance as the nominal resistance of the piezoresistive film in the displacement sensor. The voltage output of the Wheatstone bridge can be obtained as follows:

$$V_{\mathrm{out}} = \frac{V_{\mathrm{bias}}}{4}\frac{\Delta R}{R} = \frac{V_{\mathrm{bias}}}{4}\frac{G}{L_3}\frac{t_z}{(EI)_3}\int_0^{L_3}M_3(x)\,\mathrm{d}x, \tag{17}$$

where V_{bias} is the bias voltage applied to the Wheatstone bridge. In this resonator model, once the temperature of the thermal actuator is obtained, the strain of the displacement sensor can be calculated by using equations (2)–(5), the gauge factor of the displacement sensor using equations (6)–(14) and the sensor output using equations (15)–(17).

4. Finite-element simulations of the resonant sensor

Several FEM simulations are performed to verify the feasibility of the resonant sensor design, along with the development of the analytical model. In these simulations, the thermal actuator is 200 μm in length and 2 μm × 20 μm in width. The polysilicon heater is 5 μm in width. The absorption plate is 100 μm in length and 200 μm in width. The displacement sensor is 100 μm in length and 2 μm × 10 μm in width. The piezoresistive film in the displacement sensor is 2 μm in width. Thickness of the structure is obtained from the process data sheet and shown in figure 1. Table 1 lists the material properties needed for these simulations.

Figure 6 shows the first two resonant modes of the proposed resonator design. The plot reveals that the first resonant mode is the designated out-of-plane motion and the resonant frequency is 81.08 kHz; the second mode is an in-plane motion and the resonant frequency is 112.22 kHz. The frequency of the second mode is 1.4 times higher than that of

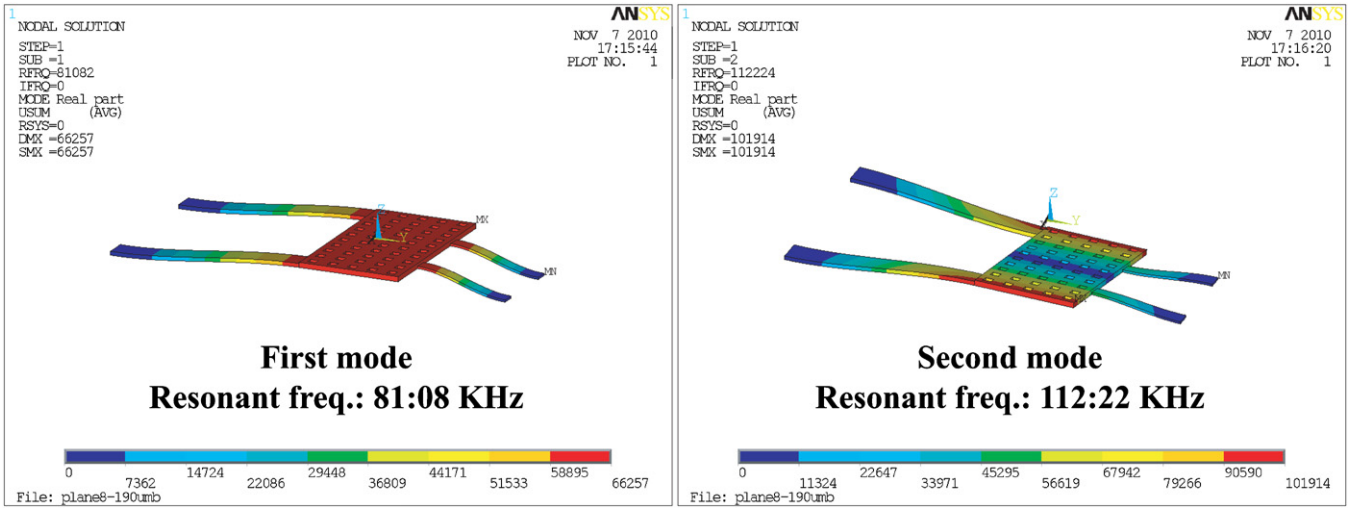

(*a*) (*b*)

Figure 6. Modal analysis of the proposed sensor design. (*a*) First mode: out-of-plane motion, 81.08 kHz. (*b*) Second mode: in-plane motion, 112.22 kHz.

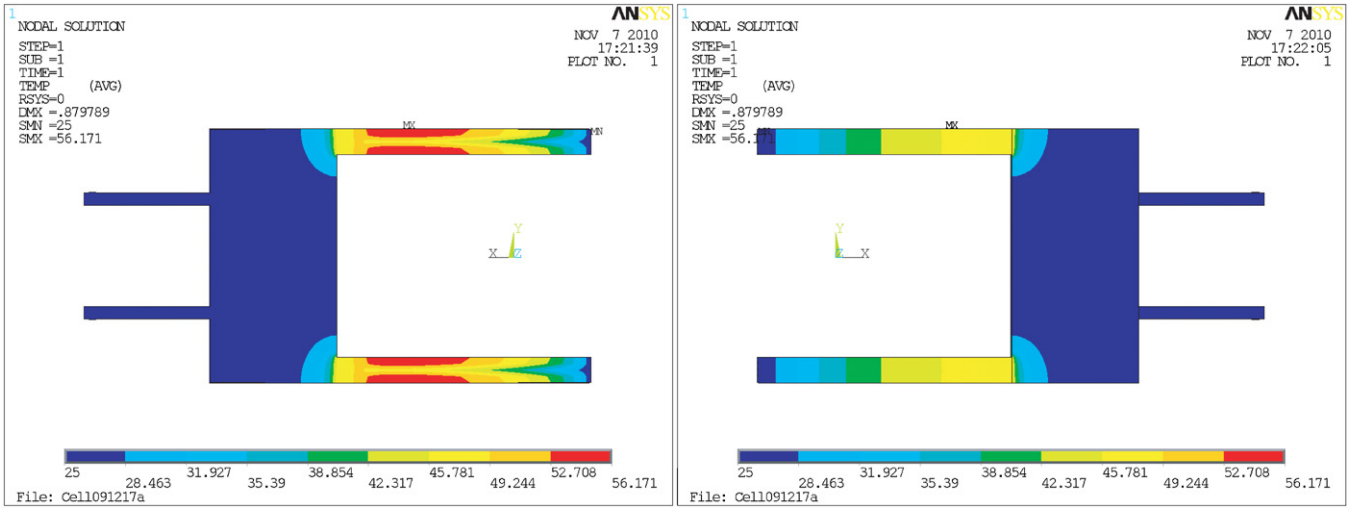

(*a*) (*b*)

Figure 7. Temperature distribution of the proposed sensor design when a dc 4 V is applied to the polysilicon heater. The highest temperature is 55 °C. (*a*) View on the rear side. (*b*) View on the front side.

the first mode. The second resonant motion should thus not interfere much with the designated motion of the plate.

Figure 7 shows the temperature distribution of the device when a dc voltage 4 V is applied to the thermal actuator. According to the simulation results, the temperature of the thermal actuator is above the room temperature (25 °C), due to the joule heating of the polysilicon heater. The polysilicon heater is designed to have a 'U' shape and is placed close to the bottom of the thermal actuator. Therefore, the maximum temperature of the resonator (56 °C) is located at the bottom of the thermal actuator and close to the tip of the thermal actuator. A large portion of the absorption plate and displacement sensor maintain their temperature at the room temperature. Therefore, the heat interference from the thermal actuator to the displacement sensor is negligible.

Based on the temperature difference of 30 °C ($\simeq$ 56 °C − 25 °C) from FEM simulation results, the deformed shape of the proposed resonator design can be predicted using the analytical model (equations (2)–(5)). Simulation results in figure 8 indicate that the analytical model and FEM model predict a similar deformed shape. Additionally, the maximum deflection is located at the tip of the displacement sensor, which is 1.48 μm predicted by the FEM model and 1.4 μm by the analytical model. The deviation from these two models is approximately 5%.

5. Device fabrication

Figure 9(*a*) presents the cross-sectional view of the device after the standard 2P4M CMOS process. The entire die is covered by the passivation layer. To manufacture different composite structures for the proposed resonant sensor design, figure 9(*b*) shows that portion of the passivation layer is first removed by one lithography ('PAD' mask [21]), followed by

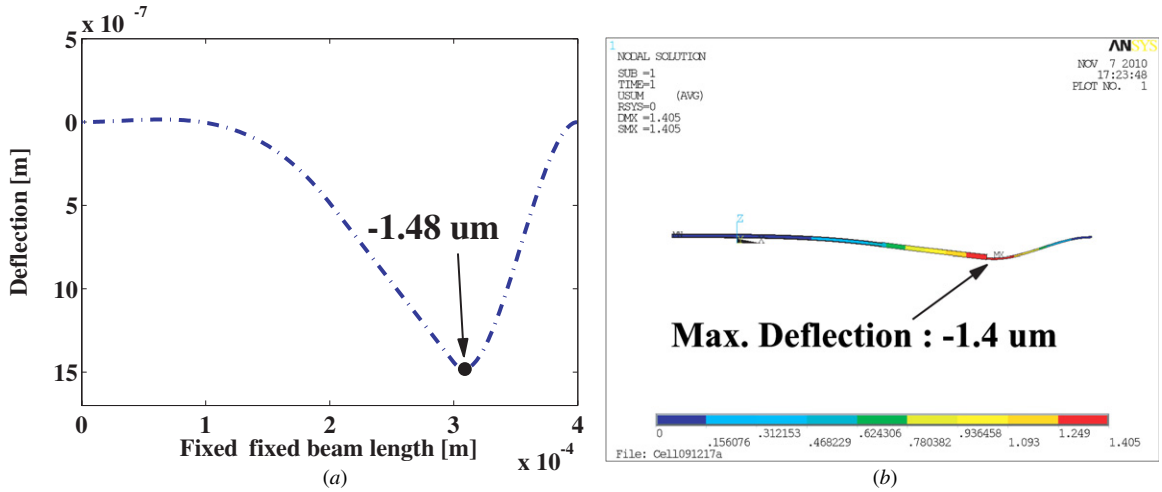

Figure 8. Simulation of the deformed shape of the proposed sensor design. (*a*) Analytical model, the maximum deflection is -1.48 μm. (*b*) FEM model, the maximum deflections is -1.4 μm.

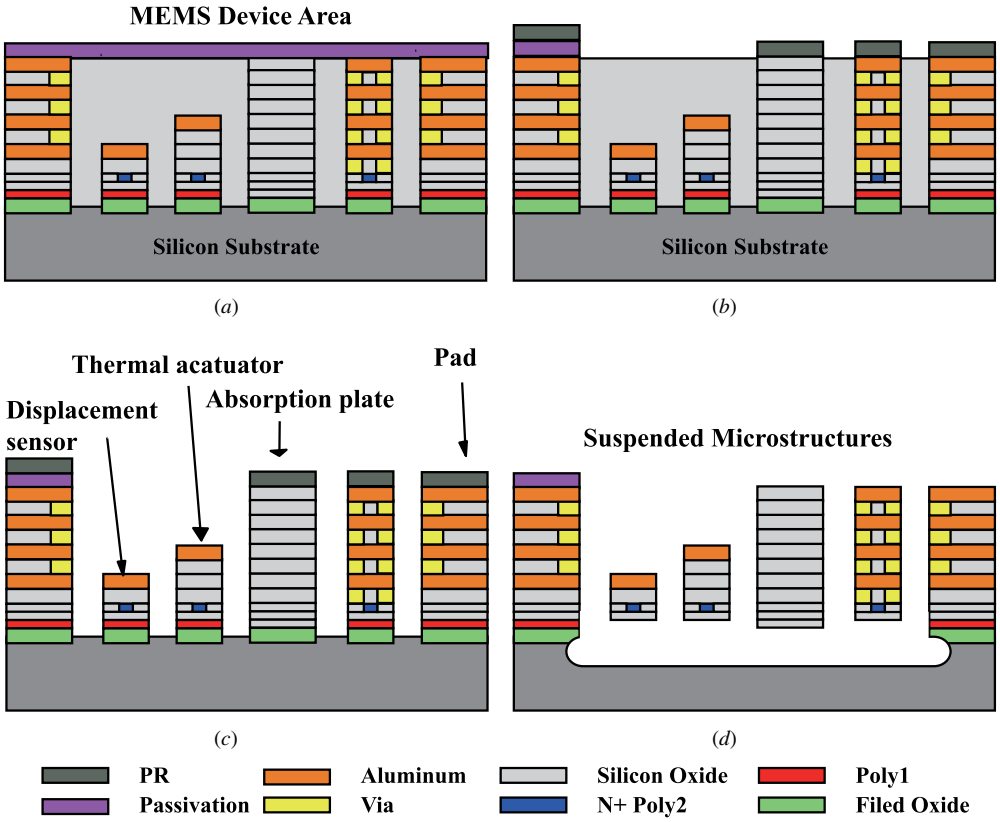

Figure 9. Fabricating the sensor design using the 2P4M CMOS process and post-CMOS process. (*a*) Completion of CMOS process. (*b*) Removing the passivation layer using 'PAD' mask and patterning the MEMS structure using 'RLS' mask. (*c*) Etching silicon dioxide by anisotropic RIE etching. (*d*) Releasing the MEMS structure by an isotropic silicon etch.

another mask ('RLS'[21]) that defines the structure sidewalls. Figure 9(*c*) presents an anisotropic reactive-ion-etch (RIE) using CHF_3/O_2 plasma. This step etches away silicon oxide and stops on metal layers and silicon substrate. According to our experience, a minimum 4 μm $\times$ 4 μm window can be successfully accomplished in this process step, which defines the minimum sidewall spacing of MEMS structures. Additionally, the polysilicon layer should be placed, at least, 2 μm away from the edges of the protection metal layer to prevent it from damage by this dry etching process. Finally, an isotropic RIE with SF_6/O_2 is applied to etch portion of the silicon substrate, subsequently releasing the MEMS structures. Following the removal of the PR mask, the fabrication process is completed. Figures 9(*c*) and (*d*) show different composite structures needed for this resonant sensor design.

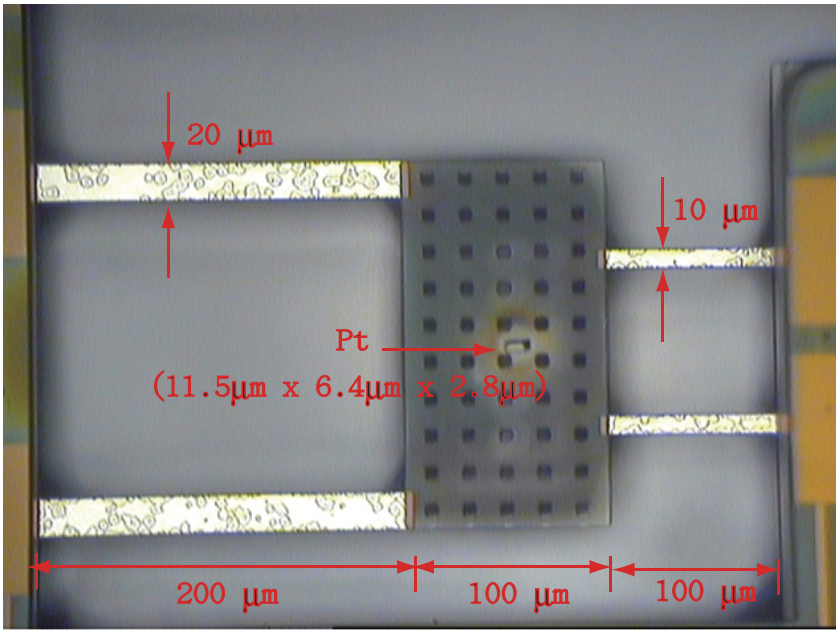

Figure 10. A fabricated device and its dimension.

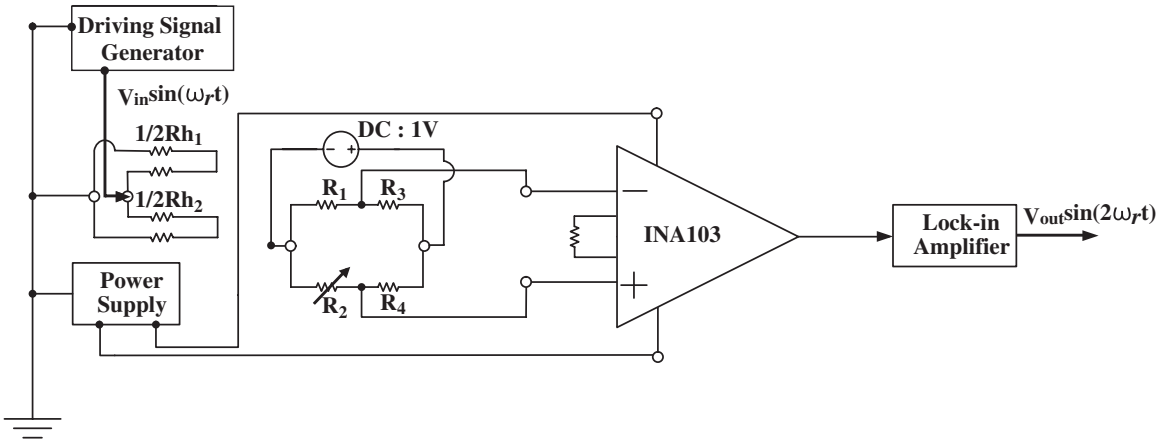

Figure 11. The block diagram of the driving circuits and Wheatstone bridge readout circuits.

6. Experimental results

The fabricated devices have the same dimensions as described in section 4, except for that the length of the displacement sensor ranges from 80 to 140 μm. Figure 10 shows one of the fabricated devices with the displacement sensor of 100 μm in length. Resistance of the polysilicon heater located at the thermal actuator is measured to be 3.8 kΩ. The piezoresistor located at the displacement sensor is measured to be 4.259 kΩ. A chunk of Pt mass is deposited on the absorption plate by using the focused ion beam for testing the resonant frequency shift. The dimensions of the Pt measured by the white-light interferometer are 11.5 μm $\times$ 6.4 μm $\times$ 2.8 μm. There exist irregular patterns on the aluminum film. Since aluminum film is a hard mask in the etching process, the thickness loss of aluminum layer is negligible [22, 23] and those irregular patterns are likely the residues from the lithography process.

Figure 11 shows the circuitry used to calibrate the fabricated devices. The proposed design consists of a Wheatstone bridge, differential pre-amplifier (INA 103) and lock-in amplifier (SIGNAL RECOVERY 7265). The Wheatstone bridge consists of four resistors, where R_2 is the designated piezoresistor located at the displacement sensor; R_1, R_3 and R_4 are fabricated resistors using the same polysilicon film as R_2 but located at a fixed substrate. $R_1 \sim R_4$ are designed to have the same resistance for the best bridge sensitivity. The bridge is biased at dc 1 V. The polysilicon heaters Rh_1 and Rh_2 in the thermal actuators are driven by a pure sinusoidal signal. Consequently, the resonator vibrates at the frequency twice that of the driving signal. Thus, the output signal frequency is twice that of the driving signal and can be measured selectively by the lock-in amplifier. Therefore, in this setup, both the electrical feedthrough effect and the resistance mismatch effect are suppressed.

Several experiments are performed to verify the effectiveness of the proposed design, which includes the piezoresistivity of the polysilicon film, temperature distribution of the resonator and resonant frequency variations.

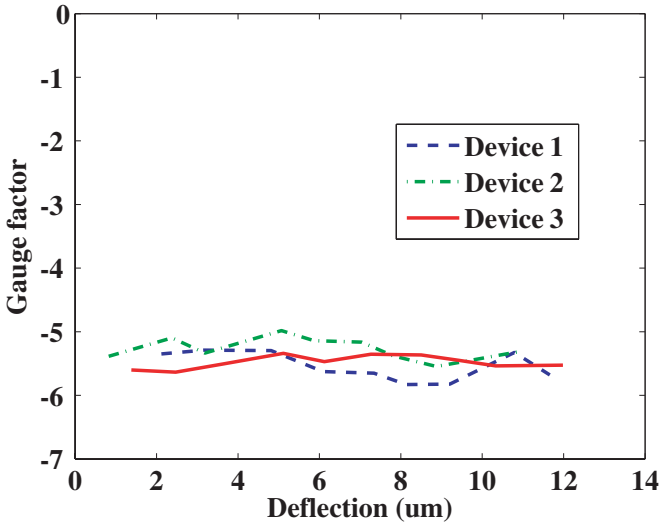

Figure 12. Calibrating the gauge factor for three piezoresistive films.

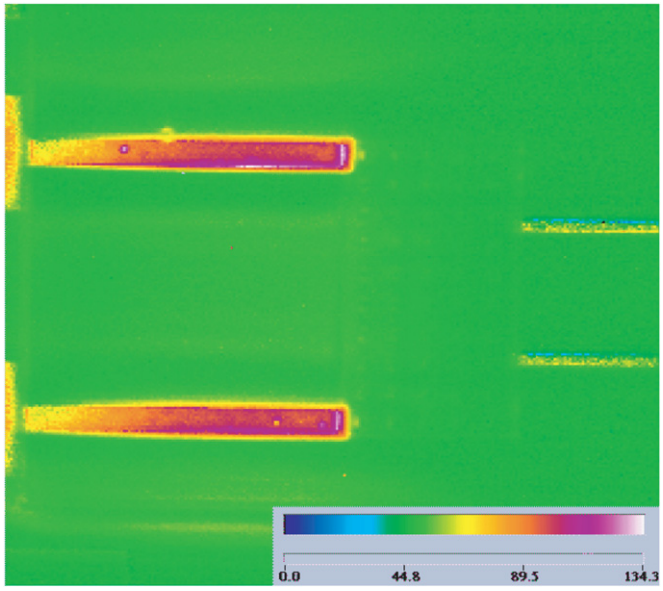

Figure 13. Static temperature distribution of the fabricated device measured by infrared. The maximum temperature is 35 °C above the background temperature.

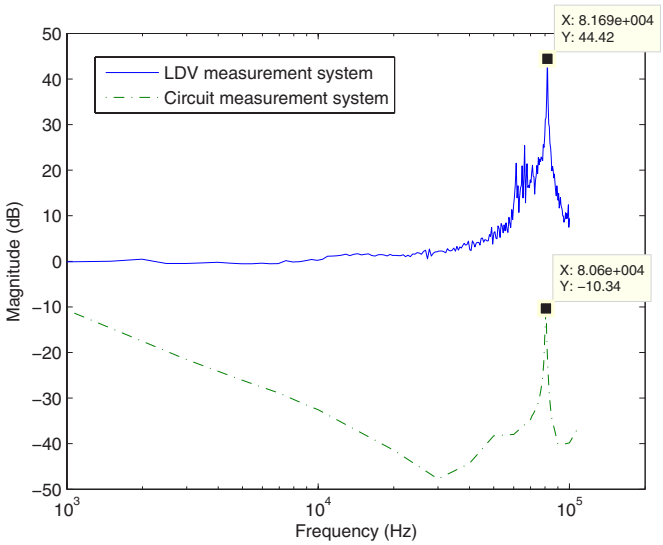

Figure 14. Resonant frequency of the device measured by two methods. One method uses shake table and LDV, and the resonant frequency is of 81.69 kHz. The other method uses proposed driving circuits and readout circuits, and the resonant frequency is of 80.6 kHz.

6.1. Piezoresistivity of the polysilicon film

In this experiment, a cantilever beam containing a piezoresistor made of polysilicon layer (poly2) is bent by a probe. Deflection of this cantilever beam is measured by an interferometer. And the resistance of the polysilicon film is measured by a multimeter. Based on equation (11) and the above experimental data, the gauge factor of this piezoresistive film can be calculated. Figure 12 shows the calculated gauge factor of three different cantilever beams at different beam deflections. According to the experimental results, the gauge factor is 5.56 on average and the resistivity of the film is 5.5 mΩ cm on average.

6.2. Temperature distribution of the resonator

Prior to the temperature measurement, the whole device is pre-heated to approximately 55 °C in order to suppress the background noise. A dc voltage of 4 V is then applied to the thermal actuator and the temperature distribution of the fabricated device is measured using infrared (InfraScope II from Quantum Focus Instruments). As shown in figure 13, the thermal actuator has an elevated temperature while the absorption plate maintains its temperature at the background temperature. The displacement sensor temperature is slightly higher than the background temperature owing to the self-heating effect of the Wheatstone bridge. Above results validate the proposed design with respect to the high thermal resistance of the absorption plate, which aims to prevent the thermal actuator from interfering the temperature of the displacement sensor. Moreover, the highest temperature occurs near at the end of the heating resistor and is measured at 90 °C, which equals to a temperature increase of 35 °C (=90 °C − 55 °C). Both the temperature distribution and highest temperature revealed in this experiment are consistent with the FEM simulation results shown in figure 7.

6.3. Resonant frequency of the resonator

Resonant frequency of the proposed device is measured using two methods. In the first method, the device is vibrated by a shake table and its displacement is measured by a laser Doppler vibrometer (LDV). After subtracting the dynamics of the table base, the frequency response of the device measured by the first method is 81.69 kHz and is shown in figure 14. In the second method, the resonator is driven by a sinusoidal voltage and the displacement signal is pickup by the readout circuit shown in figure 11. The peak-to-peak value of the driving voltage is 4 V. The resonant frequency is measured at 80.06 kHz. Above results closely correspond to the FEM simulation results shown in figure 6(*a*), which predicts the resonant frequency of the device of 81.08 kHz. In addition, figure 14 shows a '−20 dB/decade' roll-off at low frequencies

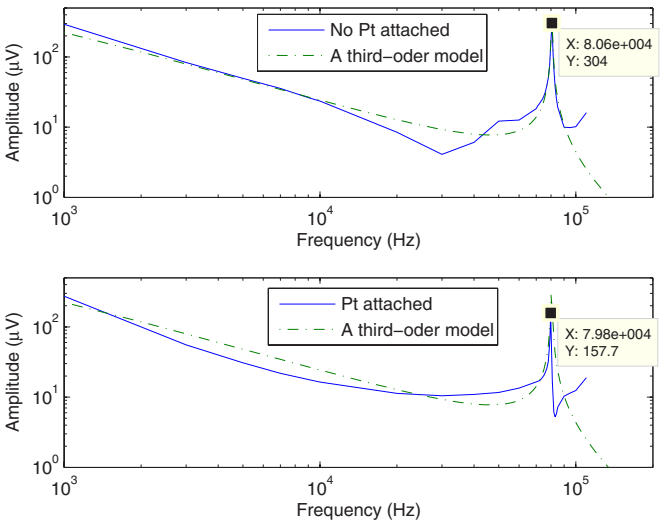

Figure 15. Resonant frequency shifts from 80.6 to 79.8 kHz when attaching a Pt mass to the absorption plate. This frequency response is measured by the circuit measurement system (second method).

for the second method but not for the first method. Other simulation results indicate that the roll-off may come from the thermal actuation, thus not showing in the first method.

6.4. Device sensitivity

Following calibration of the fabricated device, a chunk of the Pt mass is deposited on the absorption plate as shown in figure 10. After the Pt deposition, the resonant frequency of the proposed device is measured at 79.8 kHz, which is 80.06 kHz before the deposition (see figure 15). The mass of the resonator before the Pt deposition is estimated from the FEM model as 6.96×10^{-10} kg. By using the frequency shift and equation (1), the mass of the Pt is estimated to be 4.54×10^{-12} kg. The mass of the Pt, estimated by the measured dimension (see figure 10) and the Pt density of 2.145×10^3 kg m^{-3}, is 4.42×10^{-12} kg. The deviation of these two mass measurements is 2.7%. Furthermore, the sensitivity of this mass detection sensor is calculated to be 1.8×10^2 Hz ng^{-1}.

7. Discussion

According to the derivation shown in equations (6)–(10), (14), the average grain size and boundary width of a polysilicon film (microstructure) can be estimated by measuring the film resistivity and gauge factor (macro-properties) or vice versa. By using the impurity concentration of 4×10^{20} cm^{-3} (from 2P4M data sheet), boundary width of 1.5 nm and trap density at the grain boundary of 3×10^{12} cm^{-3} (used in many works [16]), figure 16 predicts the film resistivity and gauge factor as a function of the grain size. This information can be useful for industry applications because the piezoresistivity can be obtained using the in-run optical measurement instead of an intrusive calibration process. By using the results shown in figure 16, the film resistivity is predicted at (6.8 ± 2.2) mΩ cm and the gauge factor (6.8 ± 2.9) when the grain size is of (250 ± 100) nm. For comparison, several

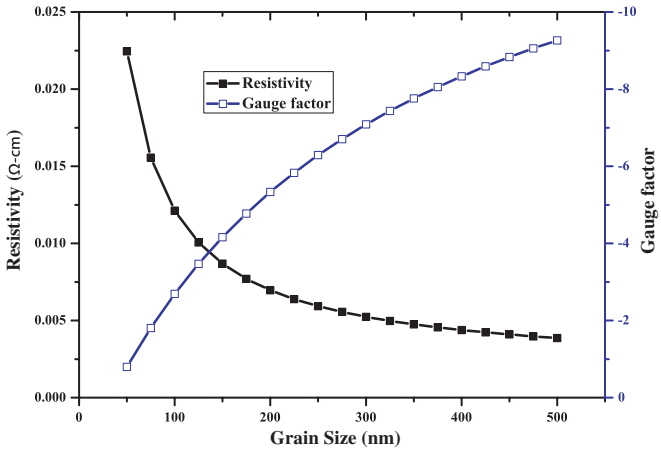

Figure 16. The relations between the grain size, resistivity, and gauge factor of a heavily doped, n-type polysilicon film, which is predicted by the derived analytical model.

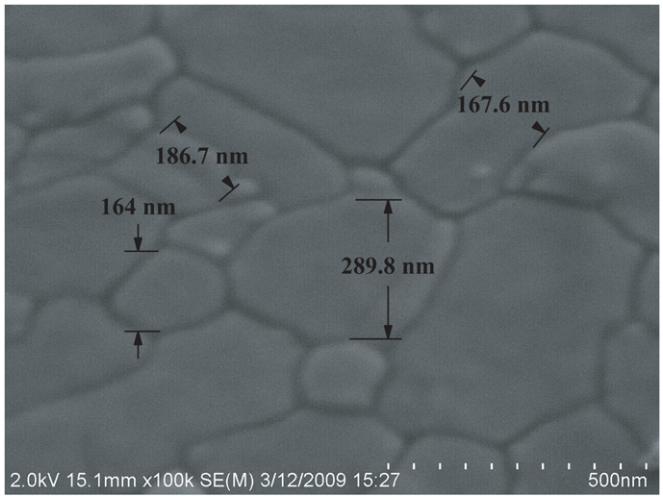

Figure 17. A SEM photo of the poly2 film in the 2P4M process. The grain size is measured to be (241 ± 105) nm.

SEM photos (see figure 17) are taken on the polysilicon film and the grain size of the film is measured to be (241 ± 105) nm. The experimental data shown in figure 12 indicate that the resistivity is of 5.5 mΩ cm on average and the gauge factor is of 5.56 on average. These experimental data validate the feasibility of the developed piezoresistance model.

The proposed design consists of many optimization problems. For example, the displacement sensor should be lengthy so that it does not destruct much of the deflection generated by the thermal actuator. However, the output signal of the piezoresistive film is proportional to the strain instead of the deflection. The lengthy design of the displacement sensor may reduce the strain, subsequently reducing the output signal. To verify this dilemma, this work fabricates devices with the same dimensions of the thermal actuator and absorption plate yet four different lengths of the displacement sensor (80, 100, 120 and 140 μm). The experimental results from these four designs are compared with the simulation results of the FEM model and analytical model. According to results shown in figure 18, the experimental results and simulation results correlate well with each other in that the output voltage

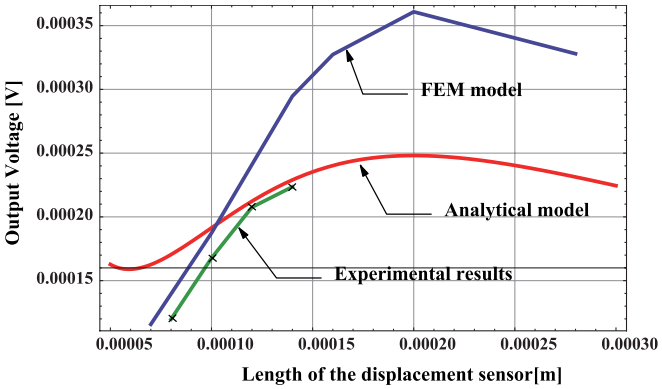

Figure 18. The relations between the length of the displacement sensor and the output signal. Experimental data and simulation results show that the output signal increases as the length of the displacement sensor increases from 80 to 140 μm. Both the FEM model and analytical model predict the optimal length of the displacement sensor of 200 μm.

increases as the length of the displacement sensor increases from 80 to 140 μm. Additionally, both FEM model and analytical model predict an optimal length of 200 μm of the displacement sensor. Unfortunately, this optimal design is not experimentally verified in this work since the current design already violates the design rule of this fabrication process for the maximum length of the suspended structure [21].

The quality factor is a key parameter of the resonator design. In this case, the quality factor excerpted from the LDV measurement is 166.3. Using this quality factor, the mass of the resonator estimated by the FEM model (6.96×10^{-10} kg), resonant frequency of the device (80.06 kHz) and a first-order system for thermal actuation, one can construct a third-order model for this thermal-actuated resonator design. For comparison purpose, the frequency response of this model is also plotted in the upper plot of figure 15 and the altered frequency response due to the additional Pt mass of 4.42×10^{-12} kg is plotted in the bottom plot of figure 15. As shown in the plot, the third-order model works well in predicting the frequency response of the resonator when no Pt mass is attached. However, the measured data show asymmetric resonant response and low quality factor (∼98) as compared to the response predicted by the model. This deviation is likely due to a non-zero background signal of the measurement system. More experiments are planned to explore the details.

8. Conclusion

This work presents the design and calibration of a thermal-actuated, piezoresistive-sensed resonant sensor fabricated by TSMC® 2P4M process. The proposed sensor design consists of three key components: thermal actuator, absorption plate and displacement sensor. The thermal actuator actuates the device into resonance. The absorption plate provides a platform for the bio-chemical reactions, subsequently changing the mass of the resonator. The additional mass changes the resonant frequency of the device and is measured by analyzing the readout signal of the piezoresistive displacement sensor.

The proposed sensor is designed by the optimal layer selection and dimension determination. For the layer selection, the thermal actuator is designed to consist of metal2-oxide-poly2-oxide films to fulfil its design goals of low thermal conductivity, large mismatched thermal coefficients and compliant bending stiffness. The absorption plate is designed to consist of four oxide films to achieve a low thermal conductivity and large bending stiffness. Moreover, the displacement sensor is designed to consist of metal1-oxide-poly2-oxide films to achieve a low bending stiffness.

This work also presents the derivation of an analytical model for determining the optimal device dimension. Based on this model, the optimal length of the displacement sensor is predicted at 200 μm when the thermal actuator is 200 μm in length and the absorption plate is 100 μm in length. Additionally, the film resistivity of the polysilicon film in the 2P4M process is predicted to be (6.8 ± 2.2) mΩ cm and the gauge factor (6.8 ± 2.9) when the grain size is (250 ± 100) nm.

Experimental results indicate that the resonant frequency of the proposed design is 80.06 kHz and shifts to 79.8 kHz when a brick of Pt mass is deposited on the absorption plate. The Pt mass estimated from the frequency shift is 4.5419×10^{-12} kg, while estimated from the measured dimension is 4.4204×10^{-12} kg. Moreover, the device sensitivity is calculated to be 1.8×10^2 Hz ng^{-1}. In this work, the grain size of the polysilicon film is measured to be (241 ± 105) nm, the resistivity is of 5.5 mΩ cm on average and the gauge factor is of 5.56 on average. Above results correlate well with the proposed analytical model. Experimental results also closely correspond to the simulation results in that the output signal of the piezoresistive sensor increases as the length of the displacement sensor increases from 80 to 140 μm. Unfortunately, this work does not experimentally confirm the optimal length of the displacement sensor of 200 μm owing to design constraints.

Acknowledgments

This research is supported by National chip implementation center (CIC) in Taiwan. We would like to express our appreciations to their great assistance.

References

[1] Brand O and Baltes H 1993 Thermally excited silicon oxide beam and bridge resonators in CMOS technology *IEEE Trans. Electron Devices* **40** 1745–53

[2] Yang H, Su S and Agogino A 2005 A resonant accelerometer with two-stage micoleverage mechanisms fabricated by SOI-MEMS technology *IEEE Sensors J.* **5** 1214–23

[3] Milovic N, Tsau C-H, Popescu G-A, Foster J-S, Burg T-P, Mirz A-R and Manalis S-R 2006 Vacuum-packaged suspended microchannel resonant mass sensor for biomolecular detection *J. Microelectromech. Syst.* **15** 1466–76

[4] Chen W-C, Yu H-T, Chen C-C, Li M-H and Li S-S 2012 Thermally-actuated and piezoresistively-sensed CMOS-MEMS resonator array using differential-mode operation *Int. Conf. on Frequency Control Symp.* pp 1–4

[5] Xu Y and Lee E-Y 2011 Feedthrough cancellation in micromechanical square resonators via differential transduction *IEEE Conf. on Electon Devices and Solid-State Circuits* pp 1–4
[6] Tuantranont A, Liew L-A and Bright V-M 2000 Modeling of thermal actuation in a bulk-micromachined CMOS micromirror *Microelectron. J.* **31** 791–801
[7] Zheng L S and Lu Michael S C 2007 A large-displacement CMOS micromachined thermal actuator with comb electrodes for capacitive sensing *Sensors Actuators* A **136** 697–703
[8] French P J 2002 Polysilicon: a versatile material for microsystems *Sensors Actuators* A **99** 3–12
[9] Kanda Y 1982 A graphical representation of the piezoresistance coefficients in silicon *IEEE Trans. Electron Devices* **ED-29** 64–70
[10] French P J and Evans A G R 1984 Piezoresistance in polysilicon *Electron. Lett.* **20** 999–1000
[11] Neamen D A 2002 *Semiconductor Physics and Devices* (New York: McGraw-Hill)
[12] Herzog C, Brand O, Lange D, Hagleitner C and Baltes H 2002 Magnetic actuation and MOS-transistor sensing for CMOS-integrated resonators *MEMS'02: Proc. 15th IEEE Int. Conf. on Micro Electro Mechanical Systems* pp 304–7
[13] Klaitabtim D and Tuantranont A 2005 Design consideration and finite element modeling of MEMS cantilever for nano-biosensor applications *5th IEEE Conf. on Nanotechnology* vol 1 pp 311–4
[14] Kirstein K-U, Hafizovic S, Lichtenberg J, Zimmermann M, Volden T and Hierlemann A 2005 A CMOS-based sensor array system for chemical and biochemical applications *ESSCIRC'05: Proc. 31st European Solid-State Circuits Conf.* pp 343–6
[15] Lu C-Y, Lu N-C, Gerzberg L and Meindl J-D 1981 Modelling and optimisation of monolithic polycrystalline silicon resistors *IEEE Trans. Electron Devices* **ED-28** 818–30
[16] Ahmed S-S, Kim D-M, Khondker A-N and Shah R-R 1984 Theory of conduction in polysilicon: Drift–diffusion approach in crystalline-amorphous-crystalline semiconductor system: part i. Small signal theory *IEEE Trans. Electron Devices* **ED-31** 480–93
[17] Wylde J and Hubbard T J 1999 Elastic properties and vibration of micro-machined structures subject to residual stresses *IEEE Canadian Conf. on Electrical and Computer Engineering 'Engineering Solutions for the Next Millennium' (Piscataway, NJ, United States)* vol 3 pp 1674–9
[18] Pallàs-Areny R and Webster J 2001 *Sensors and Signal Conditioning* (New York: Wiley)
[19] Lakdawala H and Fedder G K 1999 Analysis of temperature-dependent residual stress gradients in CMOS micromachined structures *IEEE Transducers'99* pp 526–9
[20] Kifle E-B, Raman M-S and Bhat K-N 2006 Physical model for the resistivity and temperature coefficient of resistivity in heavily doped polysilicon *IEEE Trans. Electron Devices* **53** 1885–92
[21] Chen Y-L 2006 *CIC User Handbook-0.35 um CMOS MEMS Process v.2.0* (Hsinchu, Taiwan: Chip Implementation Center)
[22] Wu P-C, Teng Y-C, Tsai H-H, Tseng S-H, Lu S-C and Juang Y-Z 2012 Implementation of a monolithic capacitive accelerometer in a wafer-level 0.18 μm CMOS MEMS process *J. Micromech. Microeng.* **22** 055010
[23] Selby J-C, Yeom J, Wu Y and Shannon M-A 2005 Maximum achievable aspect ratio in deep reactive ion etching of silicon due to aspect ratio dependent transport and the microloading effect *J. Vac. Sci. Technol.* B **23** 2319